Enhanced anomalous Nernst effects in ferromagnetic materials driven by Weyl nodes

Ilias Samathrakis[1,*] ⬤, **Teng Long**[1], **Zeying Zhang**[1,2], **Harish K Singh**[1]
and Hongbin Zhang[1] ⬤

[1] Institute of Materials Science, TU Darmstadt, 64287 Darmstadt, Germany
[2] College of Mathematics and Physics, Beijing University of Chemical Technology, Beijing 100029, People's Republic of China

E-mail: iliassam@tmm.tu-darmstadt.de

CrossMark

Abstract

Based on high-throughput (HTP) first-principles calculations, we evaluated the anomalous Hall and anomalous Nernst conductivities of 266 transition-metal-based ferromagnetic compounds. Detailed analysis based on the symmetries and Berry curvatures reveals that the origin of singular-like behavior of anomalous Hall/Nernst conductivities can be mostly attributed to the appearance of Weyl nodes or nodal lines located in the proximity of the Fermi energy, which can be further tailored by external stimuli such as biaxial strains and magnetic fields. Moreover, such calculations are enabled by the automated construction of Wannier functions with a success rate of 92%, which paves the way to perform accurate HTP evaluation of the physical properties such as the transport properties using the Wannier interpolation.

Supplementary material for this article is available online

(Some figures may appear in colour only in the online journal)

1. Introduction

In the last decades, materials of the nontrivial topological nature have attracted quite intensive attention of the community, leading to many interesting physical properties such as ultra high mobility [1], protected surface states [2], anomalous magnetoresistance [1, 3] and exotic optical properties [4], promising for future applications. One particularly interesting class of materials are those with long range magnetic orderings at finite temperatures, including topological insulators, Dirac (Weyl) semimetals (DSM, WSM) and nodal line semimetals. These materials are characterized by gapless surface Dirac fermions with a spin-momentum-locked energy dispersion, a spin-(non-)degenerate band touching point and lines respectively [5, 6]. These special energy dispersions are responsible for the generation of interesting physical phenomena. For instance, for ferromagnetic materials, where there is an imbalance of spin-up and spin-down electrons, the anomalous Hall effect (AHE) generates a transversal spin polarized charge current (charge current and spin current) in response to a longitudinal charge current, in the absence of an external magnetic field [7, 8]. The same can be achieved using the thermal gradient as the external stimulus, resulting in the anomalous Nernst effect (ANE) [9, 10]. Both AHE and ANE are caused by the nonzero Berry curvature of the Fermi sea states, [8] which acts as a fictitious magnetic field [11] giving rise to these effects that lead to promising applications such as data storage and

J. Phys. D: Appl. Phys. **55** (2022) 074003

I Samathrakis *et al*

data transfer [12, 13]. Note that like the other linear response properties, the anomalous Hall conductivities (AHCs) can also be equally evaluated by integrating the Fermi surfaces [14], arising one interesting aspect whether AHC can be tuned by external stimuli.

Recently, motivated by the emergent antiferromagnetic spintronics [15], it is demonstrated that significant AHCs and anomalous Nernst conductivities (ANCs) can be obtained in magnetic materials with noncollinear antiferromagnetic ordering [16, 17]. The most representative materials include the Mn_3X with X = Ge,Ga,Sn,Rh,In,Pt family [18–28], the Mn_3XN with X = Ga,Zn,Ag,Ni family [29–31], Mn_5Sn_3 [32, 33] and $Pr_2Ir_2O_7$ [34]. Besides AHC, the triangular noncollinear antiferromagnetic structure of the Mn_3X family is responsible for the generation of a spin current in the absence of external field, dubbed spin Hall effect (SHE) [35], the magnetic SPE [36] and the magneto-optical Kerr effect [37] which is the rotation of the plane of polarization of a light beam reflected from the surface in the presence of a magnetic field, offering interesting applications [38, 39]. Such peculiar properties can be traced back to the existence of Weyl nodes in the electronic structure [22, 40]. WSMs are topological materials where the electronic structure is dominated by non-accidental linear touching and historically $Y_2Ir_2O_7$ was the first material to be realized as a WSM [41]. Recently, $Co_3Sn_2S_2$ and several magnetic Weyl Heusler compounds were classified as WSM which also exhibit touching points with linear dispersion close to the Fermi level [42, 43], giving rise to large AHC. Therefore, there is a strong impetus to search for more magnetic WSMs and to investigate the resulting physical properties.

In this work, after collecting the known ferromagnetic materials, we performed high-throughput (HTP) calculations on the intrinsic part of the AHC and the ANC of 266 existing transition-metal-based ferromagnetic compounds, where the magnetization directions and biaxial strains are considered as perturbations to tune such effects. It is observed that the appearance of linearly degenerate states such as Weyl nodes and nodal lines will lead to singular-like behavior of AHC and hence enhanced ANC. Nevertheless, there exist also materials with significant ANC but without hot-spot contributions to AHC. Therefore, it is suspected that further HTP calculations are required in order to identify compounds with enhanced AHC and/or ANC for transversal thermoelectric applications and charge to spin-current conversion devices. Specifically, to provide promising candidates to implement techniques associated with the AHE [44], the ANE [45, 46] and magnetic damping via ANE [47], all resulting in significant advances to spin caloritronics devices.

2. Numerical details

Out of 5487 experimentally known ferromagnets, reported in AtomWork Adv database [48], the crystal structure of 3956 was found and collected using ICSD, [49] Materials Project, [50] and AtomWork databases. Compounds being either non-stoichiometric or containing elements with partial occupation were excluded, leading to 1827 compounds. Additionally, rare earths, oxides and compounds including more than 30 atoms in their unit cell were screened out as well since they increase the complexity and the time needed for the calculation. These constraints further reduced the number of available ferromagnetic compounds for calculations to 335.

The transport properties of the ferromagnetic compounds are computed automatically using an in-house-developed scheme, written in Python, linking VASP, Wannier90 and Wanniertools software. The first step involves the self consistent first-principles calculation of each compound using the projected augmented wave (PAW) method, implemented in VASP. [51] The exchange correlation functional is approximated in the general gradient approximation, as parameterized by Perdew–Burke–Ernzerhof [52] and the spin orbit coupling is included in all calculations. A Γ-centered kmesh of density 50, in respect to the lattice parameters, as well as an energy cutoff of 500 eV are selected. Subsequently, the Bloch wave functions are projected onto maximally localized Wannier functions (MLWF), using Wannier90, following [53]. The number of MLWF as well as the disentanglement and frozen windows of each compound are automatically computed following [54]. The AHC is then evaluated by integrating the Berry curvature, according to the formula:

$$\sigma_{\alpha\beta} = -\frac{e^2}{\hbar} \int \frac{d\mathbf{k}}{(2\pi)^3} \sum_n f[\epsilon(\mathbf{k}) - \mu] \Omega_{n,\alpha\beta}(\mathbf{k}), \quad (1)$$

$$\Omega_{n,\alpha\beta}(\mathbf{k}) = -2Im \sum_{m \neq n} \frac{\langle \mathbf{k}n|v_\alpha|\mathbf{k}m \rangle \langle \mathbf{k}m|v_\beta|\mathbf{k}n \rangle}{[\epsilon_m(\mathbf{k}) - \epsilon_n(\mathbf{k})]^2}, \quad (2)$$

where $f[\epsilon(\mathbf{k}) - \mu]$ denotes the Fermi distribution function, μ the Fermi energy, n (m) the occupied (empty) Bloch band, $\epsilon_n(\mathbf{k})$ ($\epsilon_m(\mathbf{k})$) their energy eigenvalues and u_α (v_β) the velocity operator. The integration is performed on 400 dense k-mesh in respect to the lattice parameters, using Wanniertools. [55] The ANC is defined according to the formula:

$$a_{\alpha\beta} = -\frac{1}{e} \int d\epsilon \frac{\partial f}{\partial \mu} \sigma_{\alpha\beta}(\epsilon) \frac{\epsilon - \mu}{T}, \quad (3)$$

where ϵ is the energy point of the energy grid, e the electron's charge, T the temperature and μ the Fermi level. Regarding the ANC, an in house developed Python script in an energy grid of 1000 points at a range $[-0.5, 0.5]$ eV in respect to the Fermi level is used.

3. Results and discussion

As stated above, starting from 335 transition-metal-based ferromagnetic materials, we managed to converge the DFT calculations for 289 compounds for both magnetization directions, i.e. the [001] and [100]. MLWFs can be successfully constructed for 266 of them, giving rise to a success rate of 92%. In comparison, a success rate of 93% and 97% is achieved in [56] and [57] respectively. Our results provide an alternative to the automatic construction of Wannier functions and enable us to perform further HTP calculations to evaluate the desired

J. Phys. D: Appl. Phys. **55** (2022) 074003

I Samathrakis *et al*
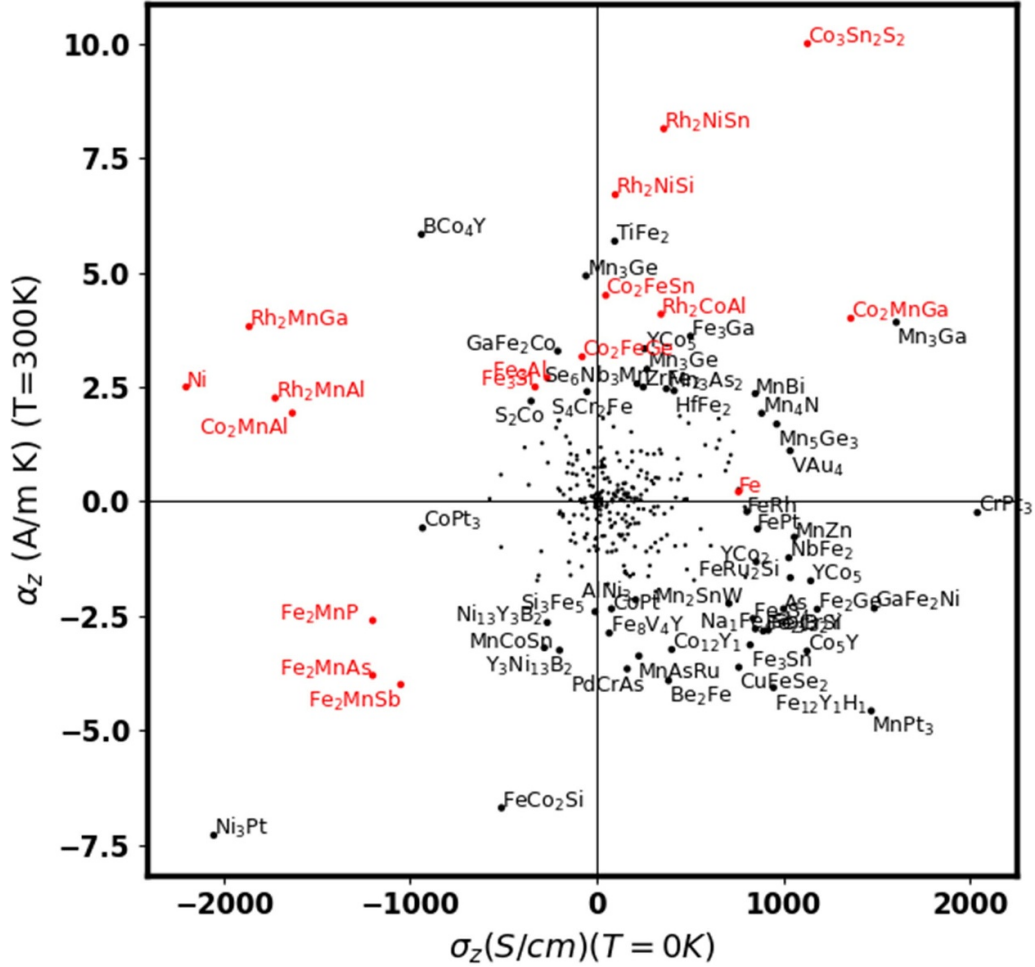
Figure 1. σ_z (at $T = 0$ K) and α_z (at $T = 300$ K) for selected ferromagnets with the magnetization direction parallel to the [001] axis. Our results are indicated with black and compared to the ones available in literature in red.

physical properties, in particular making use of the Wannier interpolation technique [58].

Figure 1 shows the *z*-component ($\sigma_z = \sigma_{xy}$) of AHC and ANC for 266 FM intermetallic compounds with the magnetization aligned along the [001] direction. Obviously, the magnitude of AHC ranges between -2051 S cm^{-1} for Ni$_3$Pt and 2040 S cm^{-1} for CrPt$_3$, where there are 11 compounds with the absolute value of AHC exceeding 1000 S cm^{-1}. The largest magnitude of AHC is larger than the already reported -1862 S cm^{-1} for Rh$_2$MnGa and -1723 S cm^{-1} for Rh$_2$MnAl [59], arising the question whether there is an upper limit and opens up the possibility to engineer materials with more significant magnitudes. Concomitant with AHC, the *z*-component ($\alpha_z = \alpha_{xy}$) of ANC varies between -7.29 A (m · K)$^{-1}$ for Ni$_3$Pt and 5.83 A (m · K)$^{-1}$ for BCo$_4$Y, and exceeds 3 A (m · K)$^{-1}$ in 16 compounds.

In general, our results match reasonably well with the existing literature for the magnetization direction being parallel to *z*-axis. More specifically the reported value of 1130 S cm^{-1} for Co$_3$Sn$_2$S$_2$ [60] is comparable with the 988 S cm^{-1} obtained from our calculations. Moreover, good agreement is achieved in Heusler compounds where our values of 140 and 200 S cm^{-1} for Co$_2$VGa and Co$_2$MnSn agree with the reported cases

of 137 S cm^{-1} in [61] and 118 S cm^{-1} in [62] respectively. Comparable results are also observed in the XPt$_3$ family with *X* = (Cr,Mn) where the reported cases of 2040 and 1400 S cm^{-1} [63] are reproduced by our values of 2000 and 1471 S cm^{-1} respectively. Regarding ANC, the calculated value of 4.58 A (m·K)$^{-1}$ for MnPt$_3$ is consistent with the reported value of 4 A (m·K)$^{-1}$ in [63]. It is important to mention that the ANC is extremely sensitive to the density of points used for the calculation as well as the temperature that might explain several differences between the reported and the calculated values.

The shape of the AHC and ANC tensors is the same and can be determined by the magnetic space group of the compound. The AHC tensor given by equation (1), primarily depends on the Berry curvature which behaves as a pseudovector under symmetry operations, yielding:

$$s\mathbf{v}(\mathbf{r}) = \pm det\left(\mathbf{D}(R)\right)\mathbf{D}(R)\mathbf{v}\left(s^{-1}\mathbf{r}\right), \qquad (4)$$

where $\mathbf{v}(r)$ denotes the pseudovector Berry curvature, $\mathbf{D}(R)$ the three-dimensional representation of a symmetry operation without the translation part and *s* an arbitrary symmetry operation. Taking SiMnY as an example, we observe that its crystal structure belongs to the space group $P4/nmm$ (129) and

the magnetization direction along the [100]-direction renders it to the magnetic space group is $Pmm'n'$ (BNS: 59.410). Correspondingly, the Berry curvature (in the Cartesian basis) behaves as an odd pseudovector under the application of m_{100} and obeys:

$$\Omega_x(-k_x, k_y, k_z) = \Omega_x(k_x, k_y, k_z)$$
$$\Omega_y(-k_x, k_y, k_z) = -\Omega_y(k_x, k_y, k_z)$$
$$\Omega_z(-k_x, k_y, k_z) = -\Omega_z(k_x, k_y, k_z).$$

Thus, the summation over the whole Brillouin zone forces $\sigma_y = \sigma_{xz}$ and $\sigma_z = \sigma_{xy}$ to vanish. On the other hand, the magnetic space group of SiMnY changes to $P4/nm'm'$ (BNS: 129.417) for the magnetization direction parallel to [001] axis. In this case, the Berry curvature behaves as an odd pseudovector under the application of 2_{100} and obeys:

$$\Omega_x(-k_x, -k_y, k_z) = -\Omega_x(k_x, k_y, k_z)$$
$$\Omega_y(-k_x, -k_y, k_z) = -\Omega_y(k_x, k_y, k_z)$$
$$\Omega_z(-k_x, -k_y, k_z) = \Omega_z(k_x, k_y, k_z).$$

It is obvious that the summation over the whole Brillouin zone forces $\sigma_x = \sigma_{yz}$ and $\sigma_y = \sigma_{xz}$ to vanish, leading to the conclusion that for the high-symmetric magnetization directions, the direction of the AHC tensor is always aligned with the magnetization direction. It is further noted that the absence of symmetries dictating specific components of the Berry curvature to be zero does not necessarily guarantee finite AHC values of the respective component, since AHC depends on the distribution of the BC in the whole BZ, originating from the band structure of the material. As a consequence, it is not forbidden for a system to exhibit an accidentally (without symmetry imposing the cancellation of BC) zero AHC value and at the same time induces nonzero ANC as it happens in P_4Fe_4 with magnetization direction parallel to x (Pn'a'2_1, BNS: 33.148, $\sigma_x = 0$, $\alpha_x = 0.12$ A$\,$(m·K)$^{-1}$), or the opposite, for a system with finite AHC value to exhibit accidentally zero ANC, as it happens in MnCo$_2$Sn (Im'm'm, BNS: 71.536, $\sigma_x = 180$ S cm^{-1}, $\alpha_x = 0$).

For magnetic materials without time-reversal symmetry, the actual symmetry and the actual electronic structure depend on the magnetization directions after considering SOC, leading to in general anisotropic responses. In order to quantify the changes in AHC and ANC, we performed calculations on two different magnetization directions, i.e. [100] and [001]. The resulting anisotropy can be expressed as the ratio of the so obtained values for the two magnetization directions, i.e. $\sigma_{x,M\|[100]}/\sigma_{z,M\|[001]}$ or $\alpha_{x,M\|[100]}/\alpha_{z,M\|[001]}$. It is clear that 'large' values signify large changes in favor of the [100] direction, as it happens for AHC and ANC in Rh$_2$MnSb and Fe$_3$Se$_4$, where anisotropy of 53.32 and -33.39 is calculated respectively. On the other hand, small values (excluding the cases where both AHC values are lower than 10 S cm^{-1} and both ANC values lower than 0.05 A$\,$(m·K)$^{-1}$ and therefore considered negligible) are in favor of the [001] magnetization direction, such as -0.01 and 0.004, that are present in PFe and Fe$_2$Ge for AHC and ANC respectively. The full list

of the values obtained for AHC, ANC and anisotropy for all ferromagnetic compounds are available in table S1 of the supplementary [66] (available online at stacks.iop.org/JPD/55/074003/mmedia). Compounds with AHC larger than or equal to 1000 S cm^{-1} (irrespective of the direction), ANC larger than or equal to 3 A$\,$(m·K)$^{-1}$ and anisotropy larger than 4 or smaller than 0.25 are classified as extreme cases and they are highlighted.

Recent works have shown that Weyl nodes and nodal lines, being bands touching points, behave either as sinks or as sources of the Berry curvature [8, 64, 65] and hence they are expected to contribute to the total AHC, the origin of which demonstrates the validity of the Mott relation. To further elucidate the origin of singular-like AHC with resulting magnificent ANC, detailed analysis is done on the energy-dependent AHC for MnZn (BNS: 123.345) (for crystal structure see figure 2(a)), as shown in figure 2(b) with the magnetization direction along the [001] axis. There exists a sharp peak of AHC about 1082 S cm^{-1} located about 4 meV below the Fermi energy. Explicit band structure analysis reveals the presence of a circularly shaped nodal line at $k_y = 0.5$ plane (red part in figure 2(d)), which further appears at the planes $k_x = \pm 0.5$, $k_z = \pm 0.5$ and $k_y = -0.5$ due to the presence of the symmetries of the compound (black and blue parts). Importantly, we found that about 73% of the total AHC (782 S cm^{-1} out of 1082 S cm^{-1}) can be attributed to the contribution of the nodal lines (figure 2(b)), similarly to the role of Weyl nodes in Mn$_3$PdN [64]. Exactly due to the presence of such nodal lines and their contribution to the singular-like AHC, the behavior of ANC around E$_F$ is dominated by the contributions from the nodal lines (figure 2(c)). Therefore, the presence of Weyl nodes and nodal lines close to the Fermi energy can lead to an anomalous energy dependence of AHC and hence enhanced ANC.

A note about the role of symmetry of the nodal lines and their contributions to AHC is in order. As discussed above, the symmetry of the Berry Curvature in the Brillouin zone is essential to understand the origin of AHC. For MnZn with the magnetization direction along the z-axis, the corresponding Magnetic Laue group $4/mm'm'$ indicates the presence of the six closed-loop-nodal lines of figure 2(d). However, not all of these symmetry equivalent nodal lines contribute equally to the same component of AHC, though their geometry are dictated by the energy eigenvalues and thus the symmetry. The underlined Laue group for the compound includes the m_z mirror plane symmetry that flips the sign of x and y components of Berry curvature while it leaves z component unchanged, according to:

$$\Omega_x(k_x, k_y, -k_z) = -\Omega_x(k_x, k_y, k_z)$$
$$\Omega_y(k_x, k_y, -k_z) = -\Omega_y(k_x, k_y, k_z)$$
$$\Omega_z(k_x, k_y, -k_z) = \Omega_z(k_x, k_y, k_z).$$

Hence, the contribution from the top black nodal ring as well as from the upper half of the red and the blue will exactly cancel out the one from the bottom black and the lower half of the red and the blue respectively for x and y components. A complete list of Berry curvature transformations with respect to each
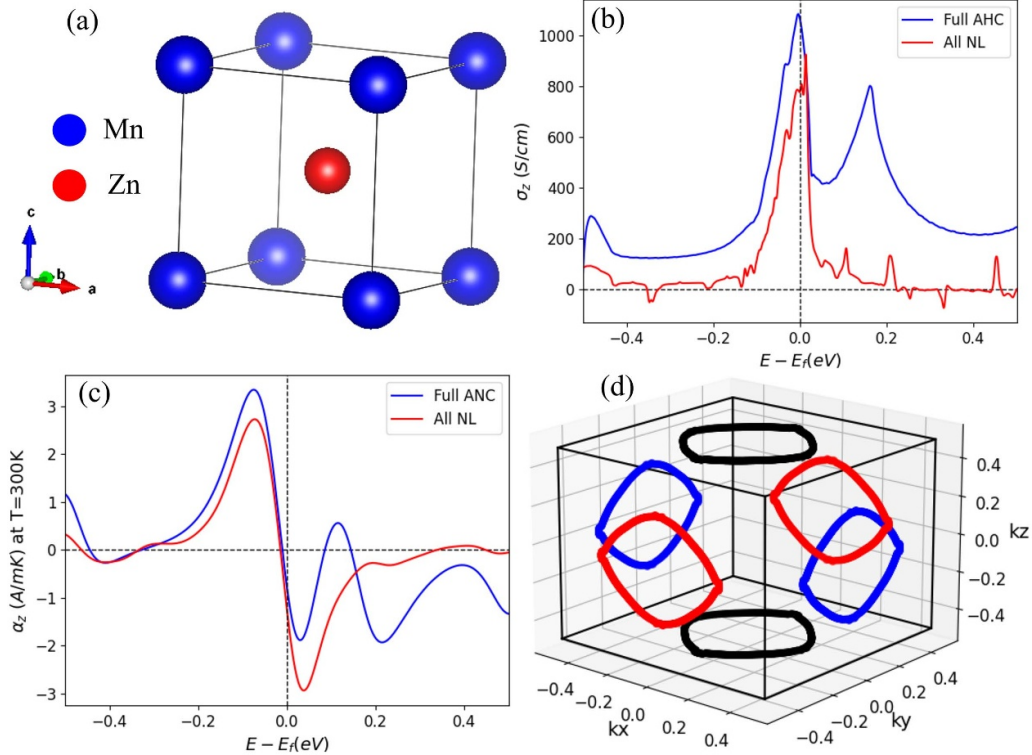
Figure 2. (a) Crystal structure of MnZn. (b) The z-component of the AHC (σ_z) (blue) and the AHC contribution originating from the nodal lines (red) as a function of energy for MnZn with magnetization direction parallel to [001] axis. (c) The z-component of the ANC (α_z) evaluated at $T = 300$ K (blue) and the ANC contribution originating from the nodal lines (red) as a function of energy for MnZn with magnetization direction parallel to [001] axis. (d) Symmetry related nodal lines of MnZn, with magnetization direction parallel to [001] axis, contributing to the total AHC value.

symmetry operation of the magnetic Laue group $4/mm'm'$ is found in table S2 of the supplementary [66].

Enhanced ANC values may originate from AHC contributions other than isolated Weyl nodes and nodal lines. The presence of nodal rings are responsible for almost 3/4 of the total AHC of MnZn, as discussed above. However, there are cases with more complicated behavior, such as Ni$_3$Pt that hosts a surprisingly large AHC of -2051 S cm^{-1} that renders it as the largest calculated AHC. In order to investigate its origin, we split the BZ ($k_i \in [-0.500, 0.500)$) in $6 \times 6 \times 6 = 216$ cubes and calculate the AHC within each of these, as illustrated in figure 3(b)). Our results show the presence of about 208 Weyl nodes within the energy range $[E_f - 0.02, E_f + 0.02]$ eV that makes the analysis of each of them separately challenging. Instead, focusing on the AHC distribution, we observe that each part of the BZ contributes to the total value, demonstrating the presence of numerous Weyl nodes, nodal lines as well as extended small band gap areas. Such areas are illustrated in the region $(k_x, k_y) \in [0.33, 0.50]$ of the band gap plot of figure 3(a). A direct comparison between figures 3(a) and (b) at these specific areas, shows that the enhanced AHC values are originating from the combination of small gap areas and the existing Weyl nodes. Despite the absence of singular-like contributions from Weyl nodes, there is a giant ANC of -7.29 A mK^{-1} (at

the Fermi energy) calculated, originating from the whole BZ, showing at the same time that large ANC values are possible.

As the Fermi level can be tuned by several mechanisms including doping and mechanical strain, it is fruitful to discuss the possibility of inducing larger AHC and ANC values away from the charge neutral point. In order to investigate the impact of such modifications to the transport properties, we consider the hexagonal compound CoSe$_4$ (BNS: 61.436) (for crystal structure see figure 4(a). Interestingly, the compound exhibits an AHC of 202 S cm^{-1} at the Fermi energy and moreover a sharp peak at almost 500 S cm^{-1}, 5 meV above (see figure 4(b)) that can be tuned by doping. Since, in general, compounds that exhibit single-valued AHC peaks close to the Fermi energy offer great opportunities for modifying AHC and hence ANC values by means of doping, some promising candidates include VAu$_4$, CoS$_2$ and Co$_2$CrAl that exhibit AHC peaks of 1955, -1048 and 1140 S cm^{-1} at 0.051, -0.024 and 0.027 eV respectively. AHC and ANC can also be modified by applying biaxial strain. That is, the tensile strain of 0.5% reduces the size of the peak to 306 S cm^{-1} and moves it at 0.01 eV in respect to the Fermi energy. On the other hand, the applied compressive strain of 1.0% has the opposite effect and hence the size of the peak is increased to 683 S cm^{-1} and its position lies at -0.001 eV (see figure 4(d)).

J. Phys. D: Appl. Phys. **55** (2022) 074003

I Samathrakis *et al*
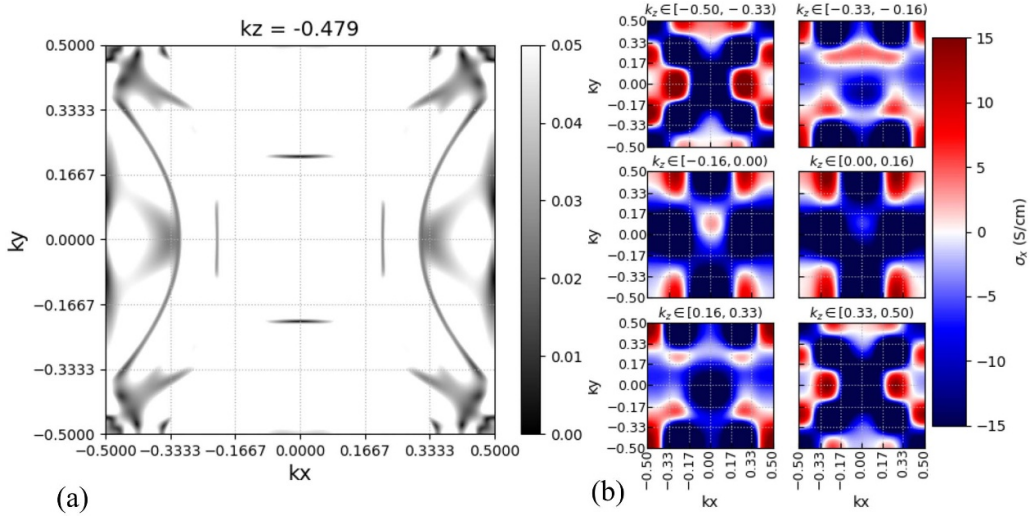
Figure 3. (a) Band gap (in eV) at a slice of Brillouin Zone ($k_z = -0.479$) for Ni$_3$Pt. (b) The *x*-component of the AHC evaluated in 216 Brillouin Zone cubes for Ni$_3$Pt with magnetization direction parallel to [100] axis.
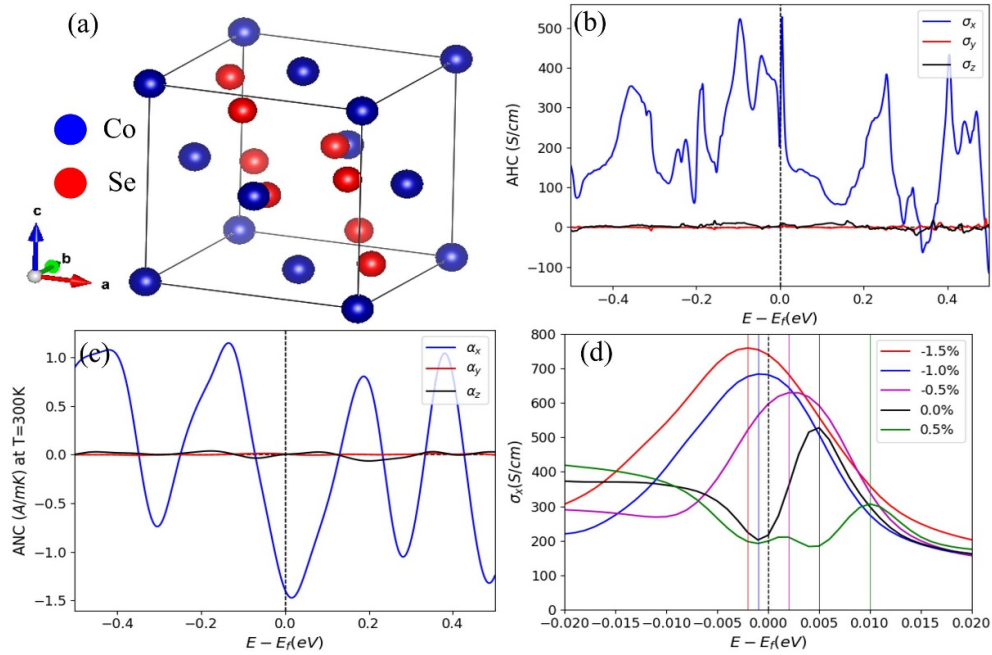
Figure 4. (a) Crystal structure of CoSe$_4$. (b) The AHC components as a function of energy for CoSe$_4$ with magnetization direction parallel to [100] axis. (c) The ANC components evaluated at $T = 300$ K as a function of energy for CoSe$_4$ with magnetization direction parallel to [100] axis. (d) The *x*-component of the AHC of CoSe$_4$ with magnetization direction parallel to [100] axis for different values of applied strain.

4. Conclusion

Based on HTP first-principles calculations, we evaluated the AHC as well as the ANC of 266 transition-metal based ferromagnets. We report that the absolute value of AHC (ANC) of 11 (16) compounds is larger than 1000 S cm^{-1} (3A (m· K)$^{-1}$) with the largest being equal to 2060 S cm^{-1} for CrPt$_3$ (-7.24A (m·K)$^{-1}$ for Ni$_3$Pt). These compounds could potentially be useful candidate materials for novel transversal thermoelectric applications. Moreover, we find that the AHC and ANC values are by 3/4 originating from linear degenerate states such as Weyl nodes and nodal lines in MnZn and they can further be enhanced by a factor of 43% by applying external stimuli, such as 1.5% compressive strain in CoSe$_4$. However, large AHC and ANC values can arise even without the presence of isolated singular hot spots in the Berry curvature but instead from uniform extended small band gap areas from the whole BZ in Ni$_3$Pt.

J. Phys. D: Appl. Phys. **55** (2022) 074003

I Samathrakis *et al*

Data availability statement

The data that support the findings of this study are available upon reasonable request from the authors.

Acknowledgments

ORCID iDs

Ilias Samathrakis ⬤ https://orcid.org/0000-0001-9754-145X
Hongbin Zhang ⬤ https://orcid.org/0000-0002-1035-8861

References

[1] Liang T, Gibson Q, Ali M N, Liu M, Cava R and Ong N 2015 Ultrahigh mobility and giant magnetoresistance in the Dirac semimetal Cd3 As2 *Nat. Mater.* **14** 280–4
[2] Xu S-Y *et al* 2015 Discovery of a Weyl fermion semimetal and topological fermi arcs *Science* **349** 613–7
[3] Huang X *et al* 2015 Observation of the chiral-anomaly-induced negative magnetoresistance in 3d Weyl semimetal TaAs *Phys. Rev.* X **5** 031023
[4] Wu L, Patankar S, Morimoto T, Nair N L, Thewalt E, Little A, Analytis J G, Moore J E and Orenstein J 2017 Giant anisotropic nonlinear optical response in transition metal monopnictide Weyl semimetals *Nat. Phys.* **13** 350–5
[5] Zhang H 2021 High-throughput design of magnetic materials (https://doi.org/10.1088/2516-1075/abbb25)
[6] Sato M and Ando Y 2017 Topological superconductors: a review *Rep. Prog. Phys.* **80** 076501
[7] Žutić I, Fabian J and Sarma S D 2004 Spintronics: fundamentals and applications *Rev. Mod. Phys.* **76** 323
[8] Nagaosa N, Sinova J, Onoda S, MacDonald A H and Ong N P 2010 Anomalous Hall effect *Rev. Mod. Phys.* **82** 1539
[9] Behnia K and Aubin H 2016 Nernst effect in metals and superconductors: a review of concepts and experiments *Rep. Prog. Phys.* **79** 046502
[10] Lee W-L, Watauchi S, Miller V, Cava R and Ong N 2004 Anomalous hall heat current and Nernst effect in the CuCr2Se4-xBrx ferromagnet *Phys. Rev. Lett.* **93** 226601
[11] Xiao D, Chang M-C and Niu Q 2010 Berry phase effects on electronic properties *Rev. Mod. Phys.* **82** 1959
[12] Hasegawa K, Mizuguchi M, Sakuraba Y, Kamada T, Kojima T, Kubota T, Mizukami S, Miyazaki T and Takanashi K 2015 Material dependence of anomalous Nernst effect in perpendicularly magnetized ordered-alloy thin films *Appl. Phys. Lett.* **106** 252405
[13] Huang S, Wang W, Lee S, Kwo J and Chien C 2011 Intrinsic spin-dependent thermal transport *Phys. Rev. Lett.* **107** 216604
[14] Wang X, Vanderbilt D, Yates J R and Souza I 2007 Fermi-surface calculation of the anomalous hall conductivity *Phys. Rev.* B **76** 195109
[15] Baltz V, Manchon A, Tsoi M, Moriyama T, Ono T and Tserkovnyak Y 2018 Antiferromagnetic spintronics *Rev. Mod. Phys.* **90** 015005
[16] Suzuki M-T, Koretsune T, Ochi M and Arita R 2017 Cluster multipole theory for anomalous Hall effect in antiferromagnets *Phys. Rev.* B **95** 094406
[17] Seemann M, Ködderitzsch D, Wimmer S and Ebert H 2015 Symmetry-imposed shape of linear response tensors *Phys. Rev.* B **92** 155138
[18] Chen H, Niu Q and MacDonald A H 2014 Anomalous Hall effect arising from noncollinear antiferromagnetism *Phys. Rev. Lett.* **112** 017205
[19] Zhang Y, Železný J, Sun Y, van den Brink J and Yan B 2018 Spin hall effect emerging from a noncollinear magnetic lattice without spin–orbit coupling *New J. Phys.* **20** 073028
[20] Nayak A K *et al* 2016 Large anomalous Hall effect driven by a nonvanishing berry curvature in the noncolinear antiferromagnet Mn3Ge *Sci. Adv.* **2** 1501870
[21] Ganguly S, Costa M, Klautau A B, Bergman A, Sanyal B, Mookerjee A and Eriksson O 2011 Augmented space recursion formulation of the study of disordered alloys with noncollinear magnetism and spin–orbit coupling: application to MnPt and Mn3Rh *Phys. Rev.* B **83** 094407
[22] Yang H, Sun Y, Zhang Y, Shi W-J, Parkin S S and Yan B 2017 Topological Weyl semimetals in the chiral antiferromagnetic materials Mn3Ge and Mn3Sn *New J. Phys.* **19** 015008
[23] Kübler J and Felser C 2014 Non-collinear antiferromagnets and the anomalous Hall effect *EPL (Europhys. Lett.)* **108** 67001
[24] Li X, Xu L, Ding L, Wang J, Shen M, Lu X, Zhu Z and Behnia K 2017 Anomalous Nernst and Righi-Leduc effects in Mn3Sn: Berry curvature and entropy flow *Phys. Rev. Lett.* **119** 056601
[25] Guo G-Y and Wang T-C 2017 Large anomalous Nernst and spin Nernst effects in the noncollinear antiferromagnets Mn$_3$x ($x =$ Sn, Ge, Ga) *Phys. Rev.* B **96** 224415
[26] Kiyohara N, Tomita T and Nakatsuji S 2016 Giant anomalous Hall effect in the chiral antiferromagnet Mn$_3$Ge *Phys. Rev. Appl.* **5** 064009
[27] Ikhlas M, Tomita T, Koretsune T, Suzuki M-T, Nishio-Hamane D, Arita R, Otani Y and Nakatsuji S 2017 Large anomalous Nernst effect at room temperature in a chiral antiferromagnet *Nat. Phys.* **13** 1085–90
[28] Železný J, Zhang Y, Felser C and Yan B 2017 Spin-polarized current in noncollinear antiferromagnets *Phys. Rev. Lett.* **119** 187204
[29] Zhou X, Hanke J-P, Feng W, Blügel S, Mokrousov Y and Yao Y 2020 Giant anomalous Nernst effect in noncollinear antiferromagnetic Mn-based antiperovskite nitrides *Phys. Rev. Mater.* **4** 024408
[30] Gurung G, Shao D-F, Paudel T R and Tsymbal E Y 2019 Anomalous hall conductivity of noncollinear magnetic antiperovskites *Phys. Rev. Mater.* **3** 044409
[31] Huyen V T N, Suzuki M-T, Yamauchi K and Oguchi T 2019 Topology analysis for anomalous Hall effect in the noncollinear antiferromagnetic states of Mn3A N (A = Ni, Cu, Zn, Ga, Ge, Pd, In, Sn, Ir, Pt) *Phys. Rev.* B **100** 094426
[32] Sürgers C, Wolf T, Adelmann P, Kittler W, Fischer G and Löhneysen H v 2017 Switching of a large anomalous Hall effect between metamagnetic phases of a non-collinear antiferromagnet *Sci. Rep.* **7** 42982
[33] Sürgers C 2018 Electrical switching of the anomalous Hall effect *Nat. Electron.* **1** 154–5
[34] Machida Y, Nakatsuji S, Maeno Y, Tayama T, Sakakibara T and Onoda S 2007 Unconventional anomalous Hall effect enhanced by a noncoplanar spin texture in the frustrated Kondo lattice Pr$_2$Ir$_2$O$_7$ *Phys. Rev. Lett.* **98** 057203
[35] Zhang Y, Sun Y, Yang H, Železný J, Parkin S P P, Felser C and Yan B 2017 Strong anisotropic anomalous Hall effect and

J. Phys. D: Appl. Phys. **55** (2022) 074003

I Samathrakis *et al*

spin Hall effect in the chiral antiferromagnetic compounds Mn3X (X = Ge, Sn, Ga, Ir, Rh and Pt) *Phys. Rev.* B **95** 075128

[36] Kimata M *et al* 2019 Magnetic and magnetic inverse spin hall effects in a non-collinear antiferromagnet *Nature* **565** 627–30

[37] Higo T *et al* 2018 Large magneto-optical Kerr effect and imaging of magnetic octupole domains in an antiferromagnetic metal *Nat. Photon.* **12** 73–8

[38] Jungwirth T, Wunderlich J and Olejník K 2012 Spin hall effect devices *Nat. Mater.* **11** 382–90

[39] Holanda J *et al* 2020 Magnetic damping modulation in IrMn3/Ni80 Fe 20 via the magnetic spin hall effect *Phys. Rev. Lett.* **124** 087204

[40] Šmejkal L, Mokrousov Y, Yan B and MacDonald A H 2018 Topological antiferromagnetic spintronics *Nat. Phys.* **14** 242–51

[41] Wan X, Turner A M, Vishwanath A and Savrasov S Y 2011 Topological semimetal and Fermi-arc surface states in the electronic structure of pyrochlore iridates *Phys. Rev.* B **83** 205101

[42] Armitage N, Mele E and Vishwanath A 2018 Weyl and Dirac semimetals in three-dimensional solids *Rev. Mod. Phys.* **90** 015001

[43] Yan B and Felser C 2017 Topological materials: Weyl semimetals *Annu. Rev. Condens. Matter. Phys.* **8** 337–54

[44] Zhou W, Yamamoto K, Miura A, Iguchi R, Miura Y, Uchida K-i and Sakuraba Y 2021 Seebeck-driven transverse thermoelectric generation *Nat. Mater.* **20** 463–7

[45] Uchida K-i, Zhou W and Sakuraba Y 2021 Transverse thermoelectric generation using magnetic materials *Appl. Phys. Lett.* **118** 140504

[46] Sakai A *et al* 2020 Iron-based binary ferromagnets for transverse thermoelectric conversion *Nature* **581** 53–7

[47] Holanda J, Santos O A and Rezende S M 2021 Thermal control of the intrinsic magnetic damping in a ferromagnetic metal *Phys. Rev. Appl.* **16** 014051

[48] Xu Y, Yamazaki M and Villars P 2011 Inorganic materials database for exploring the nature of material *Japan. J. Appl. Phys.* **50** 11RH02

[49] Hellenbrandt M 2004 The inorganic crystal structure database (ICSD)–present and future *Crystallogr. Rev.* **10** 17–22

[50] Jain A *et al* 2013 Commentary: the materials project: a materials genome approach to accelerating materials innovation *Apl. Mater.* **1** 011002

[51] Kresse G and Hafner J 1993 Ab initio molecular dynamics for liquid metals *Phys. Rev.* B **47** 558

[52] Perdew J P, Burke K and Ernzerhof M 1996 Generalized gradient approximation made simple *Phys. Rev. Lett.* **77** 3865

[53] Mostofi A A, Yates J R, Lee Y-S, Souza I, Vanderbilt D and Marzari N 2008 wannier90: a tool for obtaining maximally-localised Wannier functions *Comput. Phys. Commun.* **178** 685–99

[54] Zhang Z, Zhang R-W, Li X, Koepernik K, Yao Y and Zhang H 2018 High-throughput screening and automated processing toward novel topological insulators *J. Phys. Chem. Lett.* **9** 6224–31

[55] Wu Q, Zhang S, Song H-F, Troyer M and Soluyanov A A 2018 Wanniertools: an open-source software package for novel topological materials *Comput. Phys. Commun.* **224** 405–16

[56] Garrity K F and Choudhary K 2021 Database of Wannier tight-binding Hamiltonians using high-throughput density functional theory *Sci. Data* **8** 1–10

[57] Vitale V, Pizzi G, Marrazzo A, Yates J R, Marzari N and Mostofi A A 2020 Automated high-throughput Wannierisation *npj Comput. Mater.* **6** 1–18

[58] Marzari N, Mostofi A A, Yates J R, Souza I and Vanderbilt D 2012 Maximally localized Wannier functions: theory and applications *Rev. Mod. Phys.* **84** 1419–75

[59] Noky J, Zhang Y, Gooth J, Felser C and Sun Y 2020 Giant anomalous hall and Nernst effect in magnetic cubic Heusler compounds *npj Comput. Mater.* **6** 1–8

[60] Liu E *et al* 2018 Giant anomalous Hall effect in a ferromagnetic Kagome-lattice semimetal *Nat. Phys.* **14** 1125–31

[61] Manna K *et al* 2018 From colossal to zero: controlling the anomalous Hall effect in magnetic Heusler compounds via berry curvature design *Phys. Rev.* X **8** 041045

[62] Kübler J and Felser C 2012 Berry curvature and the anomalous Hall effect in Heusler compounds *Phys. Rev.* B **85** 012405

[63] Markou A, Gayles J, Derunova E, Swekis P, Noky J, Zhang L, Ali M N, Sun Y and Felser C 2020 Hard magnetic topological semimetals in Xpt3: harmony of berry curvature (arxiv:2008.11914)

[64] Singh H K, Samathrakis I, Fortunato N M, Zemen J, Shen C, Gutfleisch O and Zhang H 2020 Multifunctional antiperovskites driven by strong magnetostructural coupling (arxiv:2009.06440)

[65] Xu Y, Elcoro L, Song Z-D, Wieder B J, Vergniory M, Regnault N, Chen Y, Felser C and Bernevig B A 2020 High-throughput calculations of magnetic topological materials *Nature* **586** 702–7

[66] See supplemental material for Table S1 summarizing all calculated AHC, ANC, anisotropy and reported literature values for all 266 compounds and for table S2 illustrating the Berry curvature transformation under all symmetry operations of Magnetic Laue group 4/mm'm'